Volume 10 | Number 3 | 21 January 2018 | Pages 859–1548

Nanoscale

rsc.li/nanoscale

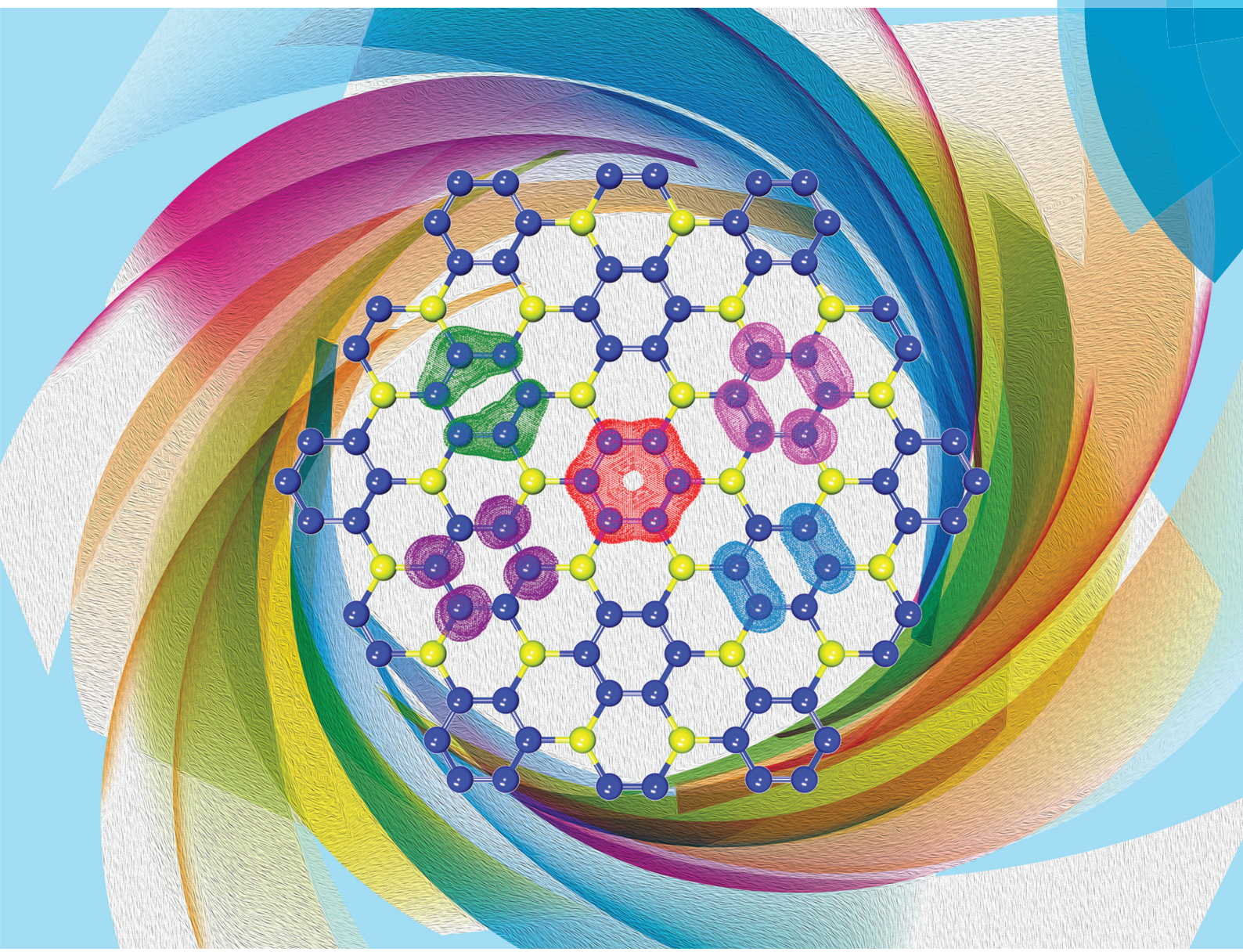

ISSN 2040-3372

ROYAL SOCIETY OF CHEMISTRY

PAPER

Qian Wang *et al.*

Stabilizing benzene-like planar N_6 rings to form a single atomic honeycomb BeN_3 sheet with high carrier mobility

NCNST

Nanoscale

PAPER

View Article Online
View Journal | View Issue

Cite this: *Nanoscale*, 2018, **10**, 949

Stabilizing benzene-like planar N_6 rings to form a single atomic honeycomb BeN_3 sheet with high carrier mobility†

Xiaoyin Li, [a,b,d] Shunhong Zhang, [c] Cunzhi Zhang [b] and Qian Wang *[a,b,d]

It is a longstanding quest to use the planar N_6 ring as a structural unit to build stable atomic sheets. However, unlike C_6H_6, the neutral N_6 ring is unstable due to the strong repulsion of the lone-pair of electrons. Using first-principles calculations and the global structure search method, we show that the N_6 unit can be stabilized by the linkage of Be atoms, forming a *h*-BeN_3 honeycomb monolayer, in which the geometry and the π-molecular orbitals of the N_6 rings are well kept. This sheet is not only energetically, dynamically and thermally stable, but also can withstand high temperatures up to 1000 K. Band structure calculation combined with a group theory analysis and a tight-binding model uncover that *h*-BeN_3 has a π-band dominated band structure with an indirect band gap of 1.67 eV. While it possesses a direct band gap of 2.07 eV at the Γ point lying in the photon energy region of visual light, its interband dipole transition is symmetrically allowed so that electrons can be excited by photons free of phonons. Based on deformation potential theory, a systematic study of the transport properties reveals that the *h*-BeN_3 sheet possesses a high carrier mobility of ~10^3 cm^2 V^{-1} s^{-1}, superior to the extensively studied transition metal dichalcogenide monolayers. We further demonstrate that this sheet can be rolled up into either zigzag or armchair nanotubes. These nanotubes are also dynamically stable, and are all direct band gap semiconductors with carrier mobility comparable to that of their 2D counterparts, regardless of their chirality and diameter. The robust stability and novel electronic and transport properties of the *h*-BeN_3 sheet and its tubular derivatives endow them with great potential for applications in nanoelectronic devices.

Received 21st October 2017,
Accepted 21st November 2017

DOI: 10.1039/c7nr07845e

rsc.li/nanoscale

Introduction

Polynitrogen molecules have been extensively studied for their potential applications as high energy density materials (HEDMs). Stabilizing polynitrogen anions in salts is an active research topic in synthetic inorganic chemistry and materials science. Recently, a breakthrough was made in the synthesis and characterization of the pentazolate anion cyclo-N_5^-,[1] which inspired us to explore other polynitrogen species. Indeed, another cyclic polynitrogen molecule – hexazine (a planar hexagon of nitrogen atoms) was also intensively studied. Vogler *et al*. claimed that hexazine can be formed in the photochemical reaction at low temperatures, 77 K,[2] which motivates studying N_6 isomers further.[3,4] However, despite the isoelectronic nature of hexazine with respect to benzene, the strong repulsion of the lone-pair of electrons on the N atoms may destabilize hexazine to decompose into three N_2 molecules.[5,6] In fact, *ab initio* calculations have confirmed that hexazine is unstable and nonaromatic even though it has six π electrons which satisfy Hückel's $(4n + 2)$ rule.[7] On the other hand, previous studies have predicted that the nitrogen atoms in metal azides, such as LiN_3,[8] NaN_3,[9] RbN_3,[10] and so on, may transform into the benzene-like N_6 ring under high pressure, but the transformation is difficult to realize experimentally because of the high pressure requirement. Thus, exploring other methods to stabilize the planar benzene-like N_6 ring is highly desirable.

Theoretical calculations indicated that introducing alkaline earth metal Ca can stabilize the planar N_6 ring through the cation–π interaction formed by electron transfer from the Ca atom to the N_6 ring.[11] However, to construct a two dimensional (2D) single atomic sheet containing the planar N_6 units, the sandwiched Ca_2N_6 cluster cannot be used. We need to find an element with Ca's electron-donating ability but an atomic size closer to N. Therefore, the element in the same main group

[a]*Center for Applied Physics and Technology, College of Engineering, Peking University; Key Laboratory of High Energy Density Physics Simulation, Ministry of Education, Beijing 100871, China. E-mail: qianwang2@pku.edu.cn*
[b]*Department of Materials Science and Engineering, College of Engineering, Peking University, Beijing 100871, China*
[c]*Institute for Advanced Study, Tsinghua University, Beijing 100084, China*
[d]*Collaborative Innovation Center of IFSA (CICIFSA), Shanghai Jiao Tong University, Shanghai 200240, China*

†Electronic supplementary information (ESI) available. See DOI: 10.1039/c7nr07845e

with Ca but having a smaller atomic size can be expected to work for this purpose. In this paper, by means of a particle-swarm optimization (PSO) based global structure search method, we have verified that Be atoms can be used to link the planar N_6 rings forming a honeycomb BeN_3 (h-BeN_3) single atomic sheet, which is the lowest-energy planar structure. By analyzing the structural stability from multiple criteria regarding thermodynamics, lattice dynamics, and thermal perturbations, we confirmed that the benzene-like N_6 rings can be stabilized in the 2D h-BeN_3 sheet under ambient conditions. We systematically studied the vibrational, mechanical, electronic and transport properties of h-BeN_3 *via* first principles calculations combined with the tight-binding method. The corresponding nanotube derivatives of the h-BeN_3 sheet are also explored.

Computational methods

The ground state structure search is performed using a particle-swarm optimization (PSO) based global structure search method implemented in the Crystal structure AnaLYsis by the Particle Swarm Optimization (CALYPSO) code,[12,13] which has been successfully employed to predict many 2D structures at given chemical compositions.[14–16] In our simulations, unit cells containing a total of 8, 16, and 20 atoms are considered. For each simulation, the structure search lasts for 20 generation loops, and in each loop 20 different structures are optimized. DFT calculations are mainly performed using the Vienna *Ab initio* Simulation Package (VASP).[17] The Projector Augmented Wave (PAW) method[18] is adopted with a kinetic energy cut off of 520 eV. The Perdew–Burke–Ernzerhof (PBE) functional[19] with the Generalized Gradient Approximation[20] is used to treat the electron exchange–correlation interactions in most calculations, while Heyd–Scuseria–Ernzerhof (HSE06)[21,22] which includes the Hartree–Fock exchange energy and the Coulomb screening effect is also used for more accurate electronic band gaps. The Brillouin zone is represented by the k point mesh following the Monkhorst–Pack scheme,[23] with a grid density of $2\pi \times 0.02$ Å^{-1}. Lattice constants and atomic positions are relaxed using the conjugated gradient algorithm without any symmetry-related constraint. The convergence threshold of total energy and atomic force components are 10^{-5} eV and 10^{-3} eV Å^{-1}, respectively. Phonon dispersion and density of states (DOS) are calculated using the finite displacement method[24] as implemented in the Phonopy code.[25] A (6×6) supercell is constructed to calculate the atomic force under finite displacements and derive the dynamics matrix. The tight-binding (TB) Hamiltonian is constructed based on the maximally localized Wannier functions (MLWFs) with the hopping parameters calculated using the Wannier90 package[26] interfaced with the Quantum ESPRESSO code.[27]

Results and discussion

Structure and stability

The most stable planar structure of BeN_3 obtained using the global structure search is shown in Fig. 1(a) (other low-energy

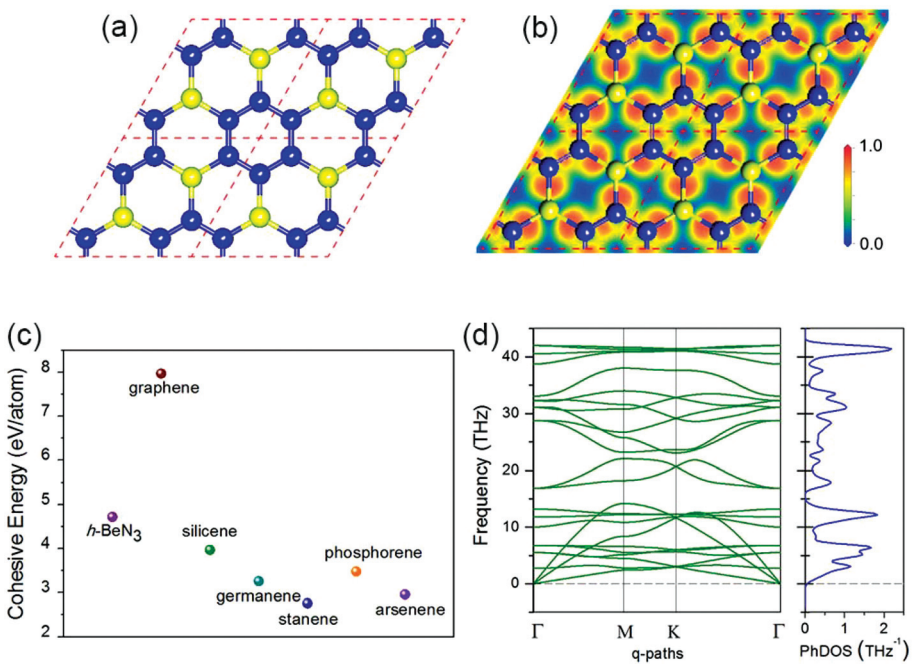

Fig. 1 (a) Optimized structure of h-BeN_3. (b) Slice of the electron localization function of h-BeN_3. Yellow and blue spheres represent Be and N atoms, respectively. The rhombus denotes the unit cell. (c) Calculated cohesive energy of h-BeN_3 and some other 2D honeycomb compounds. (d) Phonon spectra and DOS of h-BeN_3.

isomers are shown in Fig. S1†). We term it as *h*-BeN_3 because of its honeycomb lattice. Similar to graphene, *h*-BeN_3 is a flat monolayer with the highest plane symmetry of *P6mm* (plane group no. 17). Be and N atoms are located at the 2*b* (1/3, 2/3) and 6*e* (x, $-x$) 2D Wyckoff positions, respectively, with x = 0.152828. The optimized lattice constants are $a = b$ = 5.14 Å. The N–N and Be–N bond lengths are 1.36 and 1.61 Å, respectively. Interestingly, we note that *h*-BeN_3 is isostructural to the experimentally synthesized monolayer *h*-BC_3 [28] and *h*-C_3N,[29] as well as the theoretically predicted *h*-SiC_3.[30,31] However, different from those 2D compounds, *h*-BeN_3 contains planar N_6 hexagons rather than C_6 hexagons. It has been demonstrated that the charge transfer from Ca to the N_6 ring in the Ca_2N_6 cluster contributes to the structure stability.[11] Thus, we study the charge transfer and bonding nature of *h*-BeN_3 by calculating its electron localization function (ELF). From the ELF slice, as shown in Fig. 1(b), we see that the N_6 ring is electron abundant while the Be atoms are electron deficient. To get more insight, we perform the Bader charge analysis.[32] The results suggest that each Be atom transfers ~1.67 electrons to the N atoms. Consequently, each N_6 ring receives ~3.34 electrons (quite close to that of ~3.3 electrons in the Ca_2N_6 cluster[11]), which distribute uniformly on the N sites. This indicates that the N_6 ring is nearly quadruply charged like the N_6 moiety in the Ca_2N_6 cluster, which is crucial to the structural stability.

We then carefully examine the structural stability of *h*-BeN_3 from the perspectives of both energetics and dynamics. First of all, we calculate the cohesive energy of *h*-BeN_3, which is defined as $E_c = [E(\mathrm{Be}) + 3E(\mathrm{N}) - E(h\text{-}BeN_3)]/4$. The calculated cohesive energy is 4.72 eV per atom. For comparison, we calculate the cohesive energy of some other experimentally synthesized or theoretically predicted 2D honeycomb compounds using the same method and criteria of accuracy. The results are listed in Fig. 1(c). Our calculated cohesive energies of graphene, silicene, germanene, stanene, phosphorene, and arsenene are 7.97, 3.97, 3.26, 2.76, 3.48 and 2.96 eV per atom, respectively, in excellent agreement with previous studies.[33–35] The cohesive energy of *h*-BeN_3 is larger than that of experimentally synthesized 2D materials, such as silicene and phosphorene, implying the possibility of realizing such a 2D sheet.

We also calculate the formation energy of *h*-BeN_3 by using the following formula:

$$E_f(h\text{-}BeN_3) = (1/4)\mu(\mathrm{Be}) + (3/4)\mu(\mathrm{N}) - E_c(h\text{-}BeN_3), \quad (1)$$

where E_c (*h*-BeN_3) is the cohesive energy of *h*-BeN_3, and μ(Be) and μ(N) are the chemical potentials of Be and N, which are taken from the cohesive energies of hexagonal-close-packed (*hcp*) Be and N_2, respectively. The calculated formation energy of *h*-BeN_3 is 107 meV per atom. Although its formation energy is higher than that of the three-dimensional (3D) Be_3N_2 structure, it is smaller than that of the experimentally synthesized 2D g-C_3N_4 [36–38] (349 meV per atom, using graphene and N_2 as references). Moreover, it has been verified by many known 2D materials that 2D atomic sheets with a formation energy lower than 200 meV per atom are likely to exist in the freestanding form.[39] Besides, when using *hcp* Be and N_6 molecules as references, the formation energy of *h*-BeN_3 becomes −787 meV per atom. The negative value indicates that the reaction is exothermic. In this sense, it is possible to synthesize *h*-BeN_3 experimentally.

Since lattice dynamics also plays an important role in the stability of crystals, we calculate the phonon spectra of *h*-BeN_3. The results, plotted in Fig. 1(d), show that there are no imaginary modes in the entire Brillouin zone, confirming that *h*-BeN_3 is dynamically stable. For future experimental characterization, we calculate the infrared (IR) and Raman spectra corresponding to the vibration modes at the first Brillouin zone center. The calculated results in Fig. S2 (ESI†) indicate that there are two (four) peaks in the IR (Raman) spectra corresponding to four (seven) vibration modes with E_{1u} (A_{1g} or E_{2g}) symmetry.

We also perform *ab initio* molecular dynamics (AIMD) simulations to examine the thermal stability of *h*-BeN_3. A (5 × 5) hexagonal supercell (containing 200 atoms) and a ($3\sqrt{3}$ × 4) rectangle supercell (containing 192 atoms) are constructed, respectively, to perform individual AIMD simulations. After being heated at 300 K for 10 ps, the structure retains its integrity without any visible distortions, and the total potential energy fluctuates closely around the norm (see Fig. S3†), suggesting that *h*-BeN_3 is thermally stable at room temperature with the planar N_6 rings unaffected. Furthermore, our calculations show that the *h*-BeN_3 sheet can withstand temperatures as high as 1000 K (see Fig. S4†), implying the high thermal stability of the 2D structure.

Because the lattice is fixed during the AIMD simulations, we also calculate the elastic constants to study the mechanical stability of *h*-BeN_3 under small lattice distortion. Through the finite distortion approach,[40] we obtain $C_{11} = C_{22}$ = 199 N m^{-1}, C_{12} = 52 N m^{-1}, and C_{66} = 74 N m^{-1}, which satisfy the Born criteria, $C_{11} > |C_{12}| > 0$ and $C_{66} > 0$. Due to the hexagonal symmetry, the in-plane mechanical properties of *h*-BeN_3 are isotropic. From the elastic constants, we derive the Young's modulus and the Poisson's ratio to be 186 N m^{-1} and 0.26, respectively. The Young's modulus is half of that of graphene (345 N m^{-1})[41] but is larger than that of other known honeycomb sheets like H-MoS_2 (120 N m^{-1}).[42] The high in-plane stiffness of *h*-BeN_3 implies the strong bonding in the compound which is beneficial for its stability.

Electronic properties

We then explore the electronic property of *h*-BeN_3 by calculating its electronic band structure. As shown in Fig. 2(a), *h*-BeN_3 is an indirect band gap semiconductor with the valence band maximum (VBM) and conduction band minimum (CBM) located at the M and Γ points, respectively. The band gap size predicted by using the PBE functional and HSE06 hybrid functional is 1.10 eV and 1.67 eV, respectively. Moreover, the band gap at the Brillouin zone center (Γ point) is 2.07 eV at the HSE06 level, which is slightly larger than its fundamental

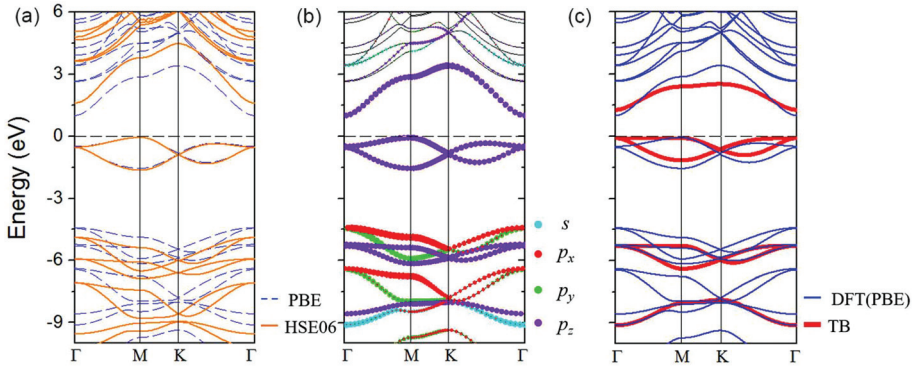

Fig. 2 (a) Electronic band structure of *h*-BeN_3. The orange solid (blue dashed) lines represent the HSE06 (PBE) results. (b) Orbital decomposed band structure of *h*-BeN_3. The size of the dots is proportional to the orbital contribution to the bands. (c) Band structure of *h*-BeN_3 derived from the TB model.

band gap (1.67 eV) but close to that of H-MoS_2 (2.13 eV)[43] and within the photon energy range of visual light.

To identify the possibility of direct optical excitation at the Γ point, we examine its dipole transition allowance. The wavefunction symmetry of the highest occupied state and the lowest unoccupied state at the Γ point are E_{2u} and B_{1g}, respectively. The point group of the Γ point is D_{6h}, according to group theory, and the dipole moment operator is $A_{2u}\oplus E_{1u}$. Accordingly, the dipole transition can be described by the following formula:

$$E_{2u} \otimes (A_{2u} \oplus E_{1u}) \otimes B_{1g} = A_{1g} \oplus A_{2g} \oplus E_{1g} \oplus E_{2g}. \quad (2)$$

We see that A_{1g} is included in the right-hand term, indicating that dipole transition is symmetry allowed at the Γ point so that electrons can be excited by photons without the assistance of phonons.

To determine the orbital composition of the energy bands, we calculate the orbital decomposed band structure of *h*-BeN_3 which is shown in Fig. 2(b). This demonstrates that the high-lying occupied bands are mainly derived from the p orbitals while the occupied bands originating from the s orbitals are deep-lying. More importantly, it shows that near the Fermi level there are six bands which are only from p_z orbitals. Therefore, it is possible and reasonable to model these electronic states using a simple TB Hamiltonian of N-p_z orbitals:

$$H = U\sum_i c_i^+ c_i + \sum_{i\neq j}(t_{ij}c_i^+ c_j + h.c.). \quad (3)$$

Here, c_i^+ and c_i represent the creation and annihilation operators of an electron in the *i*th N-p_z orbital, U is the onsite energy and t_{ij} is the hopping integral parameter between the *i*th and *j*th N-p_z orbitals. For simplicity, we only consider the nearest-neighbor intra-ring and inter-ring (the hexagonal N_6 ring) hoppings between the N-p_z orbitals, as illustrated in Fig. S5.† By fitting the DFT band structure using the MLWFs as the basis, the onsite energy U, and the intra- and inter-ring hopping integral parameters t_1 and t_2 are determined to be −3.09, −2.60 and −0.41 eV, respectively. By diagonalizing the TB model Hamiltonian, we obtain the electronic bands of *h*-BeN_3 (shown in Fig. 2(c)), which reproduce well the band alignment and dispersion features from the DFT band structure. In this sense, we have designed a π-band dominated 2D semiconductor with an intermediate band gap size between gapless graphene and wide-gap *h*-BN monolayer.

Based on the analysis of the TB model, we study the electronic structure of the N_6 moiety in *h*-BeN_3 to further understand these π-bands. Due to the high symmetry of the *h*-BeN_3 structure, the N_6 moiety maintains D_{6h} symmetry, the same as that of a freestanding N_6 cluster. Thus, we study the electronic structure of the hypothetical N_6 cluster first.

We apply the procedure of directed valence representation to illustrate how to construct π-character molecular orbitals for the hypothetical N_6 cluster. The atomic model is plotted in Fig. 3(a). From the character table presented in Table 1, the equivalence representation $\Gamma^{a.s.}$ for the six nitrogen atoms in D_{6h} symmetry can be written as $A_{1g}\oplus E_{2g}\oplus B_{1u}\oplus E_{1u}$. For the p_z orbitals which transform as A_{2u} in D_{6h} symmetry, we have the direct product represented as follows:

$$\Gamma^{a.s.} \otimes A_{2u} = A_{2u} \oplus E_{2u} \oplus B_{2g} \oplus E_{1g}. \quad (4)$$

The results indicate that there are three bonding orbitals with the symmetry of A_{2u} and E_{1g}, and three antibonding orbitals with the symmetry of E_{2u} and B_{2g}. The energy rank of the six orbitals is $B_{2g} > E_{2u} > E_{1g} > A_{2u}$. Since each N_6 moiety in *h*-BeN_3 receives ~3.34 electrons from Be atoms, there are almost ten π-electrons. As illustrated in Fig. 3(b), the ten π-electrons populate five π molecular orbitals: four of them occupy the two degenerate antibonding orbitals, and the other six π-electrons fill up the three bonding orbitals, consistent with the occupation of the π-bands in *h*-BeN_3.

For the case of *h*-BeN_3, we calculate the band decomposed charge density of these π-bands at the first Brillouin zone center. The results are plotted in Fig. 3(c). It shows that, for the five π-character occupied bands, the electron clouds are all mainly distributed on the N_6 rings and the band symmetries are the same with those of the occupied π molecular orbitals of the hypothetical N_6 cluster. For the unoccupied π band, the

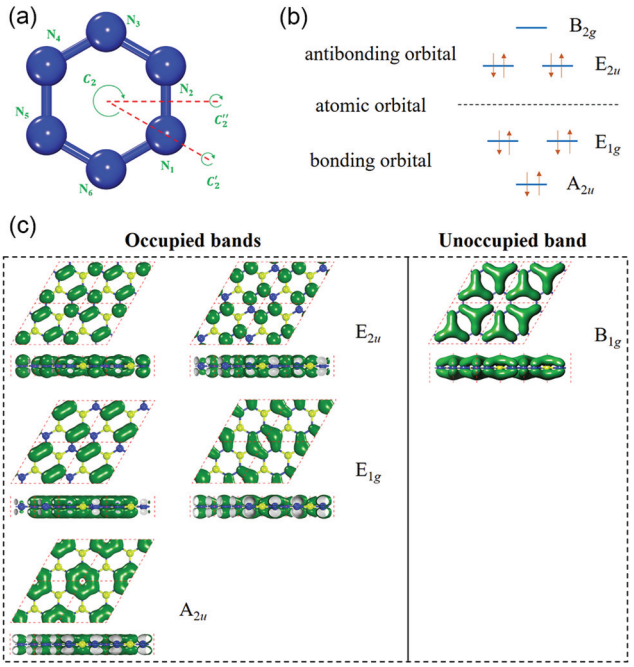

Fig. 3 (a) Atomic model of the hypothetical N_6 cluster. The two-fold rotation axes of point group D_{6h} are illustrated. (b) Diagram of π molecular orbitals derived from the p_z orbitals of N atoms. (c) The first Brillouin zone center band decomposed charge density of *h*-BeN_3, corresponding to the six π bands. The isovalue is 0.03 e Å^{-3}.

electron clouds locate both on the N atoms and Be atoms, resulting in the band symmetry differing from that of the unoccupied π molecular orbital of the hypothetical N_6 cluster. It demonstrates the well-maintained integrity of π molecular orbitals of N_6 in *h*-BeN_3, even in the presence of adjacent Be atoms.

Transport properties

Because of the moderate band gap size and the dipole allowed transition at the Brillouin zone center, we further explore the transport properties of *h*-BeN_3 for its potential electronic applications. To this end, we calculate the carrier mobility in *h*-BeN_3 using the deformation potential (DP) theory proposed by Bardeen and Shockley.[44] The analytical expression for carrier mobility (μ) of 2D semiconducting materials can be written as:

$$\mu = \frac{2e\hbar^3 C}{3k_B T|m^*|^2 {E_1}^2}, \quad (5)$$

Table 2 Deformation potential constant E_1, elastic modulus C, effective mass m^* and mobility μ for electron and hole along the zigzag and armchair directions in the *h*-BeN_3 sheet at 300 K

Carrier type		E_1 (eV)	C (N m^{-1})	m^* (m_e)	μ (×10^3 cm^2 V^{-1} s^{-1})
Electron	Zigzag	−2.25	199	0.24	9.72
	Armchair	−2.23	199	0.24	9.89
Hole	Zigzag	−2.93	199	0.51	1.27
	Armchair	−3.95	199	1.78	0.06

which has been successfully employed to study the charge transport in many 2D semiconductors, such as phosphorene,[45] monolayer MoS_2,[46] TiS_3,[47] and GeP_3.[48] Here C is the elastic modulus of the 2D sheet, T is the temperature, which is taken to be 300 K in our calculations, and $m^* = \hbar^2[\partial^2 E(k)/\partial k^2]^{-1}$ is the effective mass of the band edge carrier along the transport direction. E_1 is the DP constant defined as the energy shift of the band edge with respect to lattice dilation and compression, and k_B and $\hbar$ are Boltzmann and reduced Planck constants, respectively. Here we use an orthogonal supercell to study carrier mobilities along the zigzag and armchair directions. The atomic structure of the supercell and corresponding electronic band structure are presented in Fig. S6.† All the calculated results (m^*, E_1, C, μ) are summarized in Table 2. One can see that the electron has higher mobility than the hole in both transport directions. Thus *h*-BeN_3 can be considered an n-type semiconductor. The smaller hole mobility is primarily attributed to its larger effective mass, which can be deduced from the electronic band structure (see Fig. S6†). Remarkably, the carrier mobility in *h*-BeN_3 can be as high as 9.89×10^3 cm^2 V^{-1} s^{-1} for an electron transporting along the armchair direction, which is comparable to that of phosphorene,[45] TiS_3 [47] and GeP_3,[48] and much higher than that of monolayer MoS_2,[46] and other monolayer transition metal dichalcogenide materials,[49] indicating potential applications of *h*-BeN_3 in nanoelectronics.

Nanotube derivatives

As an extension of the current study, we investigate an important derivative of the honeycomb *h*-BeN_3 sheet, namely, the *h*-BeN_3 nanotube. We study the two main types of nanotubes, the zigzag (n, 0) and armchair (n, n) nanotubes, as illustrated in Fig. 4(a). A series of zigzag (n, 0) ($4 < n < 13$), and armchair (n, n) ($2 < n < 8$) nanotubes are systematically studied to explore their electronic properties.

First of all, we calculate the strain energies of the nanotubes, which are obtained by subtracting the total energy of the *h*-BeN_3 sheet from that of the optimized *h*-BeN_3 nanotubes.

Table 1 Characters for the $\Gamma^{a.s.}$ representation of six nitrogen atoms in the hypothetic N_6 cluster, and transformation representation of p_z orbitals (D_{6h} symmetry)

	E	$2C_6$	$2C_3$	C_2	$3C'_2$	$3C''_2$	I	$2S_3$	$2S_6$	σ_h	$3\sigma_d$	$3\sigma_v$
$\Gamma^{a.s}$ (N_6) ($A_{1g}\oplus E_{2g}\oplus B_{1u}\oplus E_{1u}$)	6	0	0	0	2	0	0	0	0	6	0	2
$\Gamma(p_z)$ (A_{2u})	1	1	1	1	−1	−1	−1	−1	−1	−1	1	1

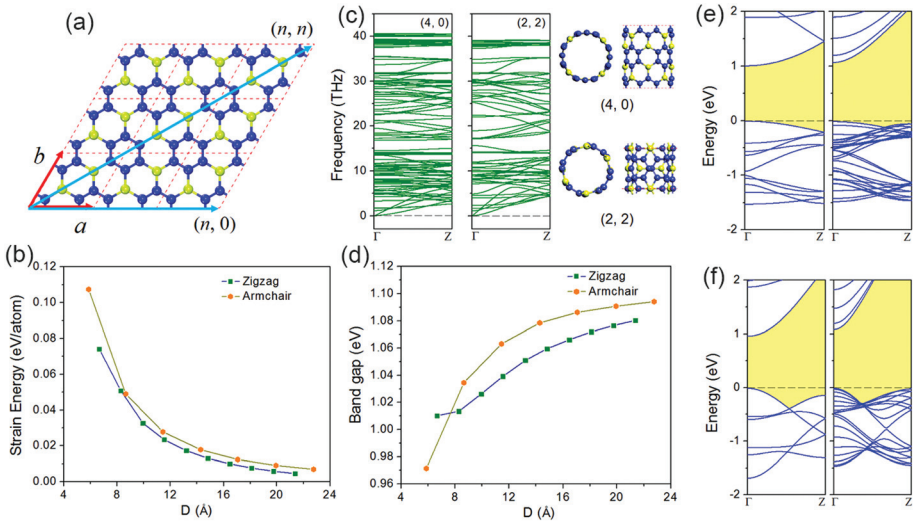

Fig. 4 (a) Illustration of the chiral vectors of two typical *h*-BeN_3 nanotubes: (*n*, 0) and (*n*, *n*) represent the zigzag and armchair, respectively. The red arrows are the lattice axes, and the cyan arrows represent the chiral vectors. (b) Strain energy *versus D* of zigzag and armchair *h*-BeN_3 nanotubes. (c) Phonon spectra and optimized structures of (4, 0) and (2, 2) *h*-BeN_3 nanotubes. (d) Variation of the band gap with diameter of zigzag and armchair *h*-BeN_3 nanotubes, respectively. (e) and (f) are the electronic band structures of zigzag (left panel: (4, 0), right panel: (13, 0)) and armchair (left panel: (2, 2), right panel: (8, 8)) *h*-BeN_3 nanotubes.

Thus, the strain energy is the energy required to roll a sheet into the corresponding nanotube, and the nanotube with smaller strain energy would have a more stable structure. The strain energies of zigzag and armchair *h*-BeN_3 nanotubes changing with diameters are plotted in Fig. 4(b), where *D* is the nanotube diameter. One can see that the strain energy decreases as the diameter increases, indicating that the nanotube with the larger diameter is more stable. Therefore, to confirm the stability, we only need to calculate the phonon spectra of the smallest nanotube, namely, the zigzag-type (4, 0)-nanotube, and the armchair-type (2, 2)-nanotube. The results are presented in Fig. 4(c). No imaginary modes exist in the entire Brillouin zone for both of the nanotubes, confirming that the studied *h*-BeN_3 nanotubes are dynamically stable.

We then study the electronic properties of *h*-BeN_3 nanotubes by calculating their electronic band structures at the PBE level. As shown in Fig. 4(d–f), with the diameter of the nanotube increasing, the band gap size gradually increases reaching that of the *h*-BeN_3 sheet (1.10 eV at the PBE level), but the gap size change is rather small. This is in contrast to other nanotubes such as phosphorene[50] or MoS_2.[51] Moreover, as opposed to the *h*-BeN_3 sheet, the nanotubes are all direct band gap semiconductors regardless of their diameters and chirality, as shown in Fig. 4(e) and (f).

By applying the zone-folding approximation,[52] we explain why all the zigzag and armchair *h*-BeN_3 nanotubes possess direct band gaps. It is known that due to the periodic boundary conditions along the circumferential direction of the nanotube, the allowed wave vectors for a given nanotube are parallel lines in the Brillouin zone of the corresponding sheet. We term these lines as the allowed **k** lines. The basic idea of the zone-folding approximation is the electronic band structure of a specific nanotube is given by the superposition of the corresponding sheet's electronic energy bands along the allowed **k** lines. Fig. 5 shows the band-folding scheme of the zigzag-type (5, 0)-nanotube and the armchair-type (5, 5)-nanotube. As illustrated in Fig. 5(a) and (c), hexagons represent the first Brillouin zone of the primitive cell of the *h*-BeN_3 sheet, while the centered rectangles are the Brillouin zone associated with the twelve-atom rectangle supercell with lattice vectors $\overrightarrow{C_h}/n = \vec{a}$ and $\vec{T} = \vec{a} - 2\vec{b}$ for a zigzag tube, $\overrightarrow{C_h}/n = \vec{a} + \vec{b}$ and $\vec{T} = \vec{a} - \vec{b}$ for an armchair tube, respectively. The thick black lines are the allowed **k** lines. Fold the corners onto the rectangular cell (cyan triangles onto the yellow ones, purple trapezoids onto the green ones) and superimpose the sheet energy bands calculated along the allowed **k** lines of length $2\pi/|\vec{T}|$, the corresponding nanotube band structure in the zone-folding approximation is then derived. One can see that, regardless of the chirality and diameter of the nanotube, the M point in the Brillouin zone of the primitive cell is folded onto the Γ point, leading to the superposition of the electronic states of the two points. From the electronic band structure of the *h*-BeN_3 sheet (Fig. 2), the VBM is located at the M point while the CBM is at the Γ point. The superposition of the two points results in the corresponding nanotube to be a direct band gap semiconductor with both the VBM and CBM located at the Γ point. This not only explains the direct band gap formation but also accounts for the minor change of band gap size when the nanotube diameter varies. Fig. 5(b)/(d) plot the calculated band structure and the zone-folding approximation derived band structure of the zigzag-type (5, 0)-nanotube/armchair-type (5, 5)-nanotube. This shows that the direct band gap

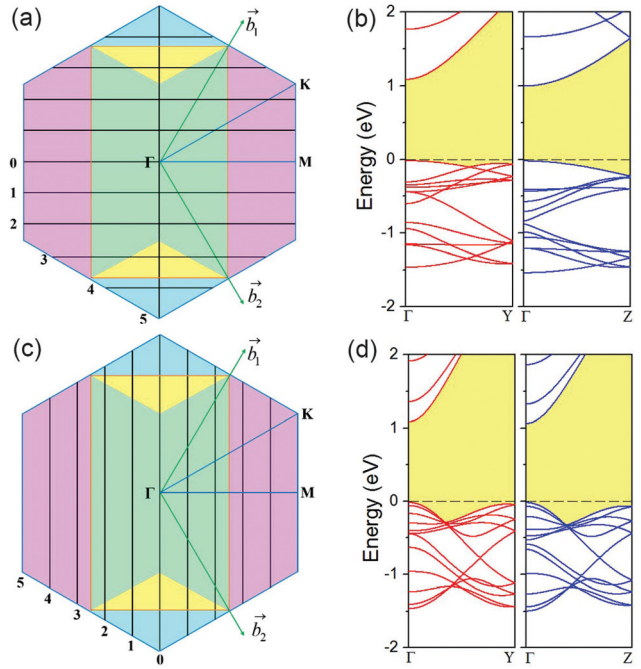

Fig. 5 (a) and (c) illustrate the zone-folding of the zigzag and armchair *h*-BeN_3 nanotubes, respectively. The thick black lines represent the allowed **k** lines for the zigzag-type (5, 0)-nanotube and the armchair-type (5, 5)-nanotube. (b) and (d) Band structures of the zigzag-type (5, 0)-nanotube and armchair-type (5, 5)-nanotube, respectively. The left panels are the derived results while the right panels are the calculated results.

characteristic of the *h*-BeN_3 nanotube is predicted accurately but the derived band structure is slightly different from that of the calculated result, which is caused by the strain introduced when the nanotube is rolled up from the 2D sheet. We can see from Fig. 5(b) and (d) that the difference between the calculated band structure and the derived result of the (5, 0)-nanotube is more obvious than that of the (5, 5)-nanotube, because the former has a larger curvature than the latter.

The carrier mobilities of the *h*-BeN_3 nanotubes are also investigated. Based on the DP theory, μ in one dimensional (1D) materials has been extensively studied by using the following formula:[46,53–56]

$$\mu = \frac{e\hbar^2 C}{(2\pi k_B T)^{1/2} |m^*|^{3/2} {E_1}^2}, \quad (6)$$

where T, m^* and E_1 are the same as those in eqn (5), while C in 1D materials is defined as $C = {z_0}^{-1} \times \partial^2 E/\partial e^2$ and z_0 is the lattice constant. From the calculated results listed in Table 3, one can see that, the electron mobility is higher than that of the hole in all studied *h*-BeN_3 nanotubes regardless of their chirality and diameters, indicating that *h*-BeN_3 nanotubes are also n-type semiconductors. The carrier mobilities in armchair *h*-BeN_3 nanotubes are all ~10^3 cm^2 V^{-1} s^{-1} for both the electron and hole, comparable to those of the 2D sheet, which is an appealing feature for applications in nanoscale electronics. The electron mobilities in zigzag type nanotubes are ~10^3 cm^2 V^{-1} s^{-1} as well, but the hole mobilities are one order smaller due to the large effective mass and DP constant. The significant difference between electron and hole mobility could be utilized for electron and hole separation in nanoelectronics.

Based on the above study, several hallmarks of the *h*-BeN_3 nanotubes are revealed: (1) the strain energy of *h*-BeN_3 nanotubes is rather small as compared to nanotubes rolled from puckered nanosheets such as phosphorene,[50] implying its synthetic viability; (2) all zigzag and armchair *h*-BeN_3 nanotubes are semiconducting with a direct band gap, and the band gap size changed mildly with respect to the tube diameter, enabling their direct application to nanoelectronics without involving chirality control or separation process that is essential for carbon nanotubes; (3) the carrier mobilities of *h*-BeN_3 nanotubes are of the order of 10^3 cm^2 V^{-1} s^{-1} and exhibit electron–hole asymmetry, suitable for n-type transport in practical electronic devices.

Table 3 Deformation potential constant E_1, elastic modulus C, effective mass m^* and mobility μ for electron and hole in zigzag and armchair *h*-BeN_3 nanotubes at 300 K

		E_1 (eV)			m^* (m_e)		μ (×10^3 cm^2 V^{-1} s^{-1})	
Nanotube type		Electron	Hole	C (eV Å^{-1})	Electron	Hole	Electron	Hole
Armchair	(4, 4)	−1.59	−1.56	205.19	0.35	0.57	3.11	1.55
	(5, 5)	−1.95	−1.99	256.68	0.31	0.55	3.10	1.26
	(6, 6)	−2.11	−2.22	308.75	0.28	0.53	3.71	1.29
	(7, 7)	−2.40	−2.59	360.16	0.27	0.53	3.53	1.10
	(8, 8)	−2.20	−2.35	411.99	0.26	0.52	5.09	1.58
Zigzag	(7, 0)	−1.18	−3.35	200.98	0.38	1.80	4.89	0.06
	(8, 0)	−1.30	−3.41	231.55	0.34	1.80	5.48	0.07
	(9, 0)	−1.50	−3.52	261.72	0.32	1.79	5.10	0.07
	(10, 0)	−1.79	−3.65	291.63	0.30	1.79	4.39	0.07
	(11, 0)	−2.07	−3.91	321.52	0.29	1.76	3.81	0.07
	(12, 0)	−2.19	−4.00	351.57	0.28	1.75	3.92	0.08
	(13, 0)	−1.86	−3.71	381.74	0.27	1.78	6.24	0.09

Conclusions

In summary, we demonstrate, using the PSO based global structure search method combined with DFT and the tight-binding method, that Be atoms can be used to stabilize the planar N_6 ring resulting in a nitrogen-rich honeycomb sheet, the *h*-BeN_3 monolayer, which is energetically, dynamically, and thermally stable. In this structure, the benzene-like N_6 ring can stably exist under ambient conditions. The in-plane mechanical properties of *h*-BeN_3 are isotropic with Young's modulus and Poisson's ratio of 186 N m^{-1} and 0.26, respectively. *h*-BeN_3 is an indirect band gap semiconductor with a band gap of 1.67 eV and a direct band gap of 2.07 eV at the Γ point, and its interband dipole transition at the Γ point is symmetrically allowed according to our group theory analysis. The Γ point band gap size and the dipole transition allowance imply the possible applications of *h*-BeN_3 in nanoelectronics. In addition, the investigation of zigzag and armchair *h*-BeN_3 nanotubes shows that the tubular derivatives are all direct band gap semiconductors. The mechanism of the indirect to direct band gap transition when going from a sheet to a nanotube is explained by applying the zone-folding approximation. More importantly, the *h*-BeN_3 sheet and the nanotubes all possess high carrier mobilities of $\sim 10^3$ cm^2 V^{-1} s^{-1}, notably higher than those of the MoS_2 monolayer and nanotubes. Electrons are found to move much faster than holes in both the sheet and nanotubes, showing the typical feature of n-type semiconductors. This work provides a strategy for the stabilization of the planar single atomic sheet composed of benzene-like N_6 rings. The robust structural stability and novel electronic and transport properties of the *h*-BeN_3 sheet and its tubular derivatives would stimulate experimental efforts for its synthesis.

Conflicts of interest

There are no conflicts to declare.

Acknowledgements

This work is partially supported by grants from the National Natural Science Foundation of China (NSFC-51471004), and the National Key Research and Development Program of China (2016YFE0127300 and 2017YFA0205003), and supported by the High Performance Computing Platform of Peking University, China.

References

1 C. Zhang, C. Sun, B. Hu, C. Yu and M. Lu, *Science*, 2017, **355**, 374.
2 A. Vogler, R. E. Wright and H. Kunkely, *Angew. Chem., Int. Ed. Engl.*, 1980, **19**, 717.
3 M. N. Glukhovtsev and P. von Ragué Schleyer, *Chem. Phys. Lett.*, 1992, **198**, 547.
4 T. M. Klapötke, *J. Mol. Struct.: THEOCHEM*, 2000, **499**, 99.
5 T.-K. Ha, R. Cimiraglia and M. T. Nguyen, *Chem. Phys. Lett.*, 1981, **83**, 317.
6 H. Huber, *Angew. Chem., Int. Ed. Engl.*, 1982, **21**, 64.
7 R. Engelke, *J. Phys. Chem.*, 1992, **96**, 10789.
8 X. Wang, J. Li, J. Botana, M. Zhang, H. Zhu, L. Chen, H. Liu, T. Cui and M. Miao, *J. Chem. Phys.*, 2013, **139**, 164710.
9 M. Zhang, K. Yin, X. Zhang, H. Wang, Q. Li and Z. Wu, *Solid State Commun.*, 2013, **161**, 13.
10 X. Wang, J. Li, N. Xu, H. Zhu, Z. Hu and L. Chen, *Sci. Rep.*, 2015, **5**, 16677.
11 H. Duan, Z. Gong, J. Cheng, W. Zhu, K. Chen and H. Jiang, *J. Phys. Chem. A*, 2006, **110**, 12236.
12 Y. Wang, J. Lv, L. Zhu and Y. Ma, *Phys. Rev. B: Condens. Matter Mater. Phys.*, 2010, **82**, 094116.
13 Y. Wang, M. Miao, J. Lv, L. Zhu, K. Yin, H. Liu and Y. Ma, *J. Chem. Phys.*, 2012, **137**, 224108.
14 Y. Li, Y. Liao and Z. Chen, *Angew. Chem., Int. Ed.*, 2014, **53**, 7248.
15 Y. Wang, F. Li, Y. Li and Z. Chen, *Nat. Commun.*, 2016, **7**, 11488.
16 C. Pu, D. Zhou, Y. Li, H. Liu, Z. Chen, Y. Wang and Y. Ma, *J. Phys. Chem. C*, 2017, **121**, 2669.
17 G. Kresse and J. Furthmüller, *Phys. Rev. B: Condens. Matter Mater. Phys.*, 1996, **54**, 11169.
18 P. E. Blöchl, *Phys. Rev. B: Condens. Matter Mater. Phys.*, 1994, **50**, 17953.
19 J. P. Perdew, K. Burke and M. Ernzerhof, *Phys. Rev. Lett.*, 1996, **77**, 3865.
20 Z. Li, P. Wu, C. Wang, X. Fan, W. Zhang, X. Zhai, C. Zeng, Z. Li, J. Yang and J. Hou, *ACS Nano*, 2011, **5**, 3385.
21 J. Heyd, G. E. Scuseria and M. Ernzerhof, *J. Chem. Phys.*, 2003, **118**, 8207.
22 J. Heyd, G. E. Scuseria and M. Ernzerhof, *J. Chem. Phys.*, 2006, **124**, 219906.
23 H. J. Monkhorst and J. D. Pack, *Phys. Rev. B: Solid State*, 1976, **13**, 5188.
24 K. Parlinski, Z. Q. Li and Y. Kawazoe, *Phys. Rev. Lett.*, 1997, **78**, 4063.
25 A. Togo and I. Tanaka, *Scr. Mater.*, 2015, **108**, 1.
26 A. A. Mostofi, J. R. Yates, Y.-S. Lee, I. Souza, D. Vanderbilt and N. Marzari, *Comput. Phys. Commun.*, 2008, **178**, 685.
27 G. Paolo, B. Stefano, B. Nicola, C. Matteo, C. Roberto, C. Carlo, C. Davide, L. C. Guido, C. Matteo, D. Ismaila, C. Andrea Dal, G. Stefano de, F. Stefano, F. Guido, G. Ralph, G. Uwe, G. Christos, K. Anton, L. Michele, M.-S. Layla, M. Nicola, M. Francesco, M. Riccardo, P. Stefano, P. Alfredo, P. Lorenzo, S. Carlo, S. Sandro, S. Gabriele, P. S. Ari, S. Alexander, U. Paolo and M. W. Renata, *J. Phys.: Condens. Matter*, 2009, **21**, 395502.
28 H. Yanagisawa, T. Tanaka, Y. Ishida, M. Matsue, E. Rokuta, S. Otani and C. Oshima, *Phys. Rev. Lett.*, 2004, **93**, 177003.

29 J. Mahmood, E. K. Lee, M. Jung, D. Shin, H.-J. Choi, J.-M. Seo, S.-M. Jung, D. Kim, F. Li, M. S. Lah, N. Park, H.-J. Shin, J. H. Oh and J.-B. Baek, *Proc. Natl. Acad. Sci. U. S. A.*, 2016, **113**, 7414.
30 Y. Ding and Y. Wang, *J. Phys. Chem. C*, 2014, **118**, 4509.
31 M. Zhao and R. Zhang, *Phys. Rev. B: Condens. Matter Mater. Phys.*, 2014, **89**, 195427.
32 E. Sanville, S. D. Kenny, R. Smith and G. Henkelman, *J. Comput. Chem.*, 2007, **28**, 899.
33 F. Matusalem, M. Marques, L. K. Teles and F. Bechstedt, *Phys. Rev. B: Condens. Matter Mater. Phys.*, 2015, **92**, 045436.
34 L.-M. Yang, I. A. Popov, T. Frauenheim, A. I. Boldyrev, T. Heine, V. Bacic and E. Ganz, *Phys. Chem. Chem. Phys.*, 2015, **17**, 26043.
35 C. Kamal and M. Ezawa, *Phys. Rev. B: Condens. Matter Mater. Phys.*, 2015, **91**, 085423.
36 M. Groenewolt and M. Antonietti, *Adv. Mater.*, 2005, **17**, 1789.
37 F. Goettmann, A. Fischer, M. Antonietti and A. Thomas, *Angew. Chem., Int. Ed.*, 2006, **45**, 4467.
38 X. Wang, K. Maeda, A. Thomas, K. Takanabe, G. Xin, J. M. Carlsson, K. Domen and M. Antonietti, *Nat. Mater.*, 2009, **8**, 76.
39 A. K. Singh, K. Mathew, H. L. Zhuang and R. G. Hennig, *J. Phys. Chem. Lett.*, 2015, **6**, 1087.
40 Y. Le Page and P. Saxe, *Phys. Rev. B: Condens. Matter Mater. Phys.*, 2002, **65**, 104104.
41 C. Lee, X. Wei, J. W. Kysar and J. Hone, *Science*, 2008, **321**, 385.
42 Q. Peng and S. De, *Phys. Chem. Chem. Phys.*, 2013, **15**, 19427.
43 M. Kan, J. Y. Wang, X. W. Li, S. H. Zhang, Y. W. Li, Y. Kawazoe, Q. Sun and P. Jena, *J. Phys. Chem. C*, 2014, **118**, 1515.
44 J. Bardeen and W. Shockley, *Phys. Rev.*, 1950, **80**, 72.
45 J. Qiao, X. Kong, Z.-X. Hu, F. Yang and W. Ji, *Nat. Commun.*, 2014, **5**, 4475.
46 Y. Cai, G. Zhang and Y.-W. Zhang, *J. Am. Chem. Soc.*, 2014, **136**, 6269.
47 J. Dai and X. C. Zeng, *Angew. Chem., Int. Ed.*, 2015, **54**, 7572.
48 Y. Jing, Y. Ma, Y. Li and T. Heine, *Nano Lett.*, 2017, **17**, 1833.
49 Z. H. Jin, X. D. Li, J. T. Mullen and K. W. Kim, *Phys. Rev. B: Condens. Matter Mater. Phys.*, 2014, **90**, 045422.
50 H. Guo, N. Lu, J. Dai, X. Wu and X. C. Zeng, *J. Phys. Chem. C*, 2014, **118**, 14051.
51 J. Xiao, M. Q. Long, X. M. Li, H. Xu, H. Huang and Y. L. Gao, *Sci. Rep.*, 2014, **4**, 4327.
52 J.-C. Charlier, X. Blase and S. Roche, *Rev. Mod. Phys.*, 2007, **79**, 677.
53 M.-Q. Long, L. Tang, D. Wang, L. Wang and Z. Shuai, *J. Am. Chem. Soc.*, 2009, **131**, 17728.
54 S. Yu, H. Zhu, K. Eshun, A. Arab, A. Badwan and Q. L. Li, *J. Appl. Phys.*, 2015, **118**, 164306.
55 W. Li, G. Zhang, M. Guo and Y.-W. Zhang, *Nano Res.*, 2014, **7**, 518.
56 M. Long, L. Tang, D. Wang, Y. Li and Z. Shuai, *ACS Nano*, 2011, **5**, 2593.